Petroleum Science 20 (2023) 460–473

Contents lists available at ScienceDirect

Petroleum Science

journal homepage: www.keaipublishing.com/en/journals/petroleum-science

Original Paper

A synthetical geoengineering approach to evaluate the largest hydraulic fracturing-induced earthquake in the East Shale Basin, Alberta

Gang Hui [a, b], Zhang-Xin Chen [a, b, *], Zheng-Dong Lei [c], Zhao-Jie Song [a], Lin-Yang Zhang [d], Xin-Ran Yu [e], Fei Gu [c]

[a] State Key Laboratory of Petroleum Resources and Prospecting, China University of Petroleum, Beijing, 102249, PR China
[b] Department of Chemical and Petroleum Engineering, University of Calgary, Calgary, AB, T2N1N4, Canada
[c] Research Institute of Petroleum Exploration and Development, Beijing, 10083, PR China
[d] School of Environmental and Municipal Engineering, Qingdao University of Technology, Qingdao, 257000, Shandong, PR China
[e] College of Pipeline and Civil Engineering, China University of Petroleum (East China), Qingdao, 266580, Shandong, PR China

ARTICLE INFO

Article history:
Received 24 November 2022
Received in revised form
9 January 2023
Accepted 9 January 2023
Available online 10 January 2023

Edited by Yan-Hua Sun

Keywords:
Geoengineering
Hydraulic fracturing
Induced seismicity
Fault reactivation
Mitigation strategies
East Shale Basin

ABSTRACT

On 2019-03-04, the largest induced earthquake (M_L4.18) occurred in the East Shale Basin, Alberta, and the underlying physical mechanisms have not been fully understood. This paper proposes a synthetical geoengineering methodology to comprehensively characterize this earthquake caused by hydraulic fracturing. Based on 3D structural, petrophysical, and geomechanical models, an unconventional fracture model is constructed by considering the stress shadow between adjacent hydraulic fractures and the interactions between hydraulic and natural fractures. Coupled poroelastic simulations are conducted to reveal the triggering mechanisms of induced seismicity. It is found that four vertical basement-rooted faults were identified via focal mechanisms analysis. The brittleness index (*BI*) along two horizontal wells has a high magnitude ($BI > 0.5$), indicating the potential susceptibility of rock brittleness. Due to the presence of overpressure, pre-existing faults in the Duvernay Formation are highly susceptible to fault reactivation. The occurrence of the earthquake clusters has been attributed to the fracturing fluid injection during the west 38^{th}-39^{th} stage and east 38^{th} stage completions. Rock brittleness, formation overpressure, and large fracturing job size account for the nucleation of earthquake clusters, and unconventional natural-hydraulic fracture networks provide fluid flow pathways to cause fault reactivation. This workflow can be used to mitigate potential seismic risks in unconventional reservoirs in other fields.

1. Introduction

The fact that hydraulic fracturing operations during the development of unconventional resources triggered induced earthquakes has received worldwide concerns from both the public and scientific communities in the last decade (Schultz et al., 2020; Lei et al., 2017; Tan et al., 2020; Ghofrani and Atkinson, 2020). In contrast to a seismically active region (e.g., the Fox Creek region) in the West Shale Basin (WSB) (Hui and Gu, 2022; Schultz et al., 2018; Shen et al., 2019; Zhang et al., 2019), the East Shale Basin (ESB) was seismically quiet as of 2018 (Schultz and Wang, 2020). However, recent hydraulic fracturing operations of multistage horizontal wells near Red Deer, Alberta, have triggered a number of induced earthquakes with large seismicity magnitudes (Wang et al., 2020). On 2019-03-04, the largest induced earthquake in the ESB thus far, the local magnitude (M_L) 4.18 event, was detected near two N–S-oriented horizontal wells (Fig. 1a). Such an event exceeds the traffic light protocol (i.e., M_L4.0) and hence received widespread scientific and public concerns (Alberta Energy Regulator, 2015). Intriguingly, the horizontal wells in the ESB were fractured with comparable fluid injection volumes (e.g., mainly 1039–1460 m^3 per stage), but only the stimulation of the two horizontal wells near Red Deer city triggered the red-light event (Fig. 1a). Despite some attempts to reveal the underlying physical mechanisms of these earthquakes, a

* Corresponding author. State Key Laboratory of Petroleum Resources and Prospecting, China University of Petroleum, Beijing, 102249, PR China.
E-mail address: zhachen@ucalgary.ca (Z.-X. Chen).

https://doi.org/10.1016/j.petsci.2023.01.006

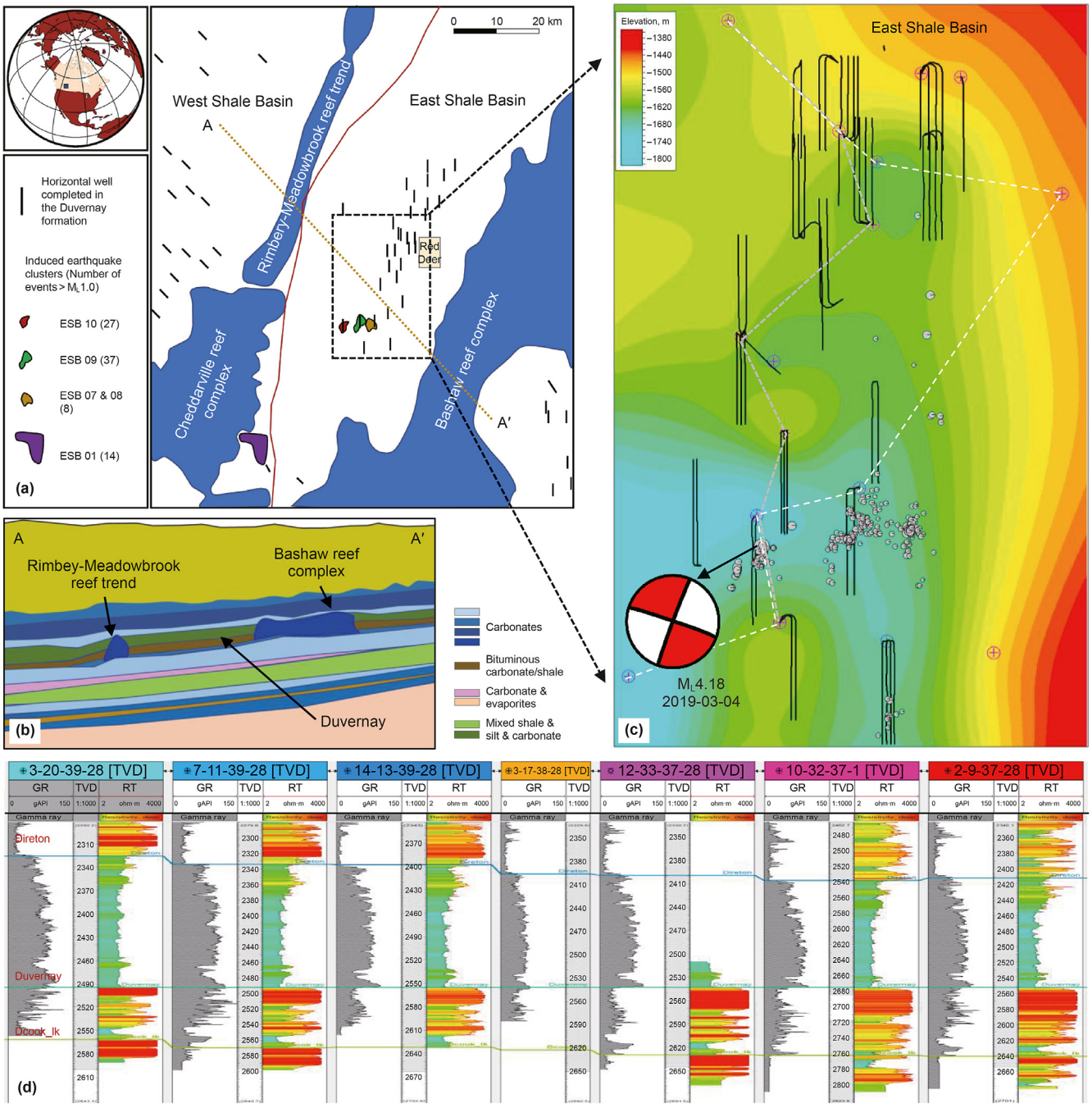

Fig. 1. The geological and seismicity information near Red Deer in Duvernay Eastern Shale Basin. (**a**) Map view of ESB. The dashed box denotes the examined region. (**b**) Associated formations developed in ESB. (**c**) Map view of recorded seismicity and drilled wells. The base map shows the elevation of the Duvernay Formation. The grey magnitude-scaled circles denote the recorded earthquakes. The beachball shows the focal mechanism of the M_L4.18 earthquake (2019-03-04). The grey dashed line shows the profile in Fig. 1d, and the white dashed line denotes the profile in Fig. 6a. (**d**) Stratigraphic correlation of straight wells showing the distinctive logging response of different formations. GR-gamma ray; RT-formation resistivity.

deterministic approach to characterizing hydraulic fracturing-induced earthquakes through the integration of geology and fracturing engineering is quite rare (Wang et al., 2020; Hui et al., 2021b, 2023; Konstantinovskaya et al., 2021).

Increased pore pressure, poroelastic stress perturbation, and aseismic fault slip are the classical triggering mechanisms for hydraulic fracturing-induced earthquakes (Ellsworth, 2013; Eyre et al., 2019). To determine the distinctive underlying mechanisms, a geoengineering approach is required to comprehensively characterize a reservoir structure (i.e., a formation, natural fractures, and pre-existing faults), petrophysical and geomechanical features, as well as the hydraulic fracture propagation (Weng et al., 2011; Hui et al., 2022a). Such an approach is extremely difficult because it involves an experimental characterization of reservoir properties and an analysis of natural-hydraulic fracture networks (Weng et al., 2014). Previous research either assigned empirical values to reservoir parameters or simply assumed a single hydraulic fracture per stage during fracturing stimulations (Pawley et al.,

2018; Hui et al., 2021a). Under this assumption, the empirical values of reservoir parameters cannot precisely depict the spatial heterogeneity of reservoir properties. Moreover, a single hydraulic fracture per stage also fails to represent the complex fracture networks beneath the ground, especially considering the interactions between hydraulic fractures and natural fractures, as well as the stress shadow effects between adjacent hydraulic fractures. Therefore, the goal of this work is to achieve a reliable experimental characterization of reservoir properties and a precise analysis of natural-hydraulic fracture networks and to reveal the underlying mechanism of the largest hydraulic fracturing-induced earthquake in the East Shale Basin.

This paper proposes a novel synthetical geoengineering methodology to comprehensively characterize the M_L4.18 earthquake caused by hydraulic fracturing. We started with building a 3D structural model using stratigraphic correlations, seismic interpretations, and analysis of focal solutions. Petrophysical measurements are then used to develop a 3D petrophysical model, while velocity and density logs are used to develop a 1D rock mechanical model. This poroelastic strain model is used to build a 3D geomechanical model. Consideration is given to the stress shadow between adjacent hydraulic fractures as well as the interactions between hydraulic and natural fractures when constructing an unconventional fracture model. Coupled poroelastic simulations are conducted under the guidance of the linear poroelasticity theory to quantify the spatial and temporal pressure and stress changes and to reveal the triggering mechanisms of induced seismicity.

2. Field background

The Devonian Duvernay Formation in Alberta, Canada, extended from the Peace River Arch in the north all the way to the Eastern Shelf carbonate platform and the Killam Barrier Reef in the south (Lyster et al., 2017). This formation is an organic-rich formation deposited in a marine basin environment. Biogenic reefs developed in their north and northwest, while carbonate terraces were generated in the southeast and west (Rokosh et al., 2012). The reef belts divide the Duvernay Formation into the East Shale Basin and West Shale Basin, and the latter is the main exploration area. The examined region is located in the south of the ESB (Fig. 1a). The Duvernay Formation in the studied region was deposited underlying a shale-hosted DIreton formation and above a shale-carbonates-interlayered Dcook_lk formation, with its formation thickness being almost constant (i.e., 42 m on average) based on its characteristic logging features (Fig. 1b–d).

The fracturing operations of two horizontal wells (6-20-37-1 and 10-20-37-1) were performed with a zipper fracturing pattern from their toe northward to their heel (Fig. 2a and b). At the time of the M_L4.18 event nucleation (i.e., 2019-03-04 12:55:17), 39 stages of the west well and 38 stages of the east well had been completed, with the total fluid injection volumes of 54,239 m^3 and 54,504 m^3, respectively (Fig. 2c). In addition, high-resolution data from broadband seismometers and nodal geophones detected 417 induced events (Wang et al., 2020). The spatial distributions of these events are depicted in Fig. 2a and b. Some significant events occurred within the Duvernay Formation, whereas others were dispersed several hundred meters below or above the stimulating play. In the map view, these events appear as four clusters (C1 through C4) with a northeast-southwest trend. The *b* values, the slopes of seismicity frequency and magnitude, of C1, are 0.59 ± 0.04 with an estimated magnitude of completeness (M_c) of 1.0 (Fig. 2d), indicating reactivations of pre-existing faults (e.g., $b < 1.5$) rather than hydraulic fracture activation (e.g., $b > 1.5$). Furthermore, the *b* values of C2 and C4 are not available due to their small number of events, and the magnitude of C3 is all below the M_c. The solutions to these focal mechanisms are available to the public (Wang et al., 2020), providing additional information on fault reactivation and natural fracture development.

3. Methods

The goal of this work, as mentioned in the Introduction Section, is to achieve a reliable experimental characterization of reservoir properties and a precise analysis of natural-hydraulic fracture networks, and to reveal the underlying mechanism of the largest hydraulic fracturing-induced earthquake in the East Shale Basin. Because building the structural model provides the understanding of pre-existing natural fractures and faults, and constructing the petrophysical and geomechanical model provides the basis for fluid diffusion and stress perturbation during fracturing operations, hence building such three high-resolution models is essential to reveal the underlying mechanisms of induced seismicity.

In this study, an integrated geoengineering approach is proposed to characterize the 4.18-magnitude earthquake triggered by hydraulic fracturing. We begin with building a 3D structural model by the stratigraphic correlations from well logging, the pre-existing fault identification from 3D seismic data, and the pre-existing natural fractures recognition from focal solutions of mainshocks. The petrophysical measurements are further used to set up a 3D petrophysical model based on the logging interpretations. Moreover, the velocity and density logs are used to derive a 1D rock mechanical model. This poroelastic strain model is employed to obtain the minimum and maximum principal stress and hence construct a 3D geomechanical model. The natural fracture networks are determined by the focal mechanisms of induced earthquakes. Considering the stress shadow between adjacent hydraulic fractures as well as the interactions between hydraulic and natural fractures, an unconventional fracture model is built to characterize the non-uniform fracture networks in unconventional reservoirs. Guided by the linear poroelasticity theory, the coupled poroelastic modeling and simulation are conducted to quantify the 4D spatial and temporal stress and pressure changes surrounding the seismogenic fault. The underlying physical mechanisms are finally determined based on the Mohr-Coulomb Failure criterion. The details of such a workflow are shown in Fig. 3.

3.1. Structural modeling

According to the characteristic logging responses in the Duvernay Formation, the top and bottom of the formation are determined by the fine stratigraphic correlations of straight wells. The ant-tracking method is used to identify the pre-existing faults associated with the induced earthquakes using high-resolution, three-dimensional seismic data (Pedersen et al., 2002). The focal solutions of induced events determine the pre-existing natural fractures within the regional tectonic setting. Combining the distributions of natural fractures and faults with stratigraphy data, we construct a fine structural model of the studied region, which serves as the structural foundation for the subsequent petrophysical model (Anyim and Gan, 2020; Chen et al., 2021).

3.2. Petrophysical modeling

A tight rock analysis (TRA) of coring wells measures their effective porosity, gas permeability, and gas saturation (Zoback, 2007). Eq. (1) below is used to calculate the effective porosity of other wells based on their well logging and core measurements.

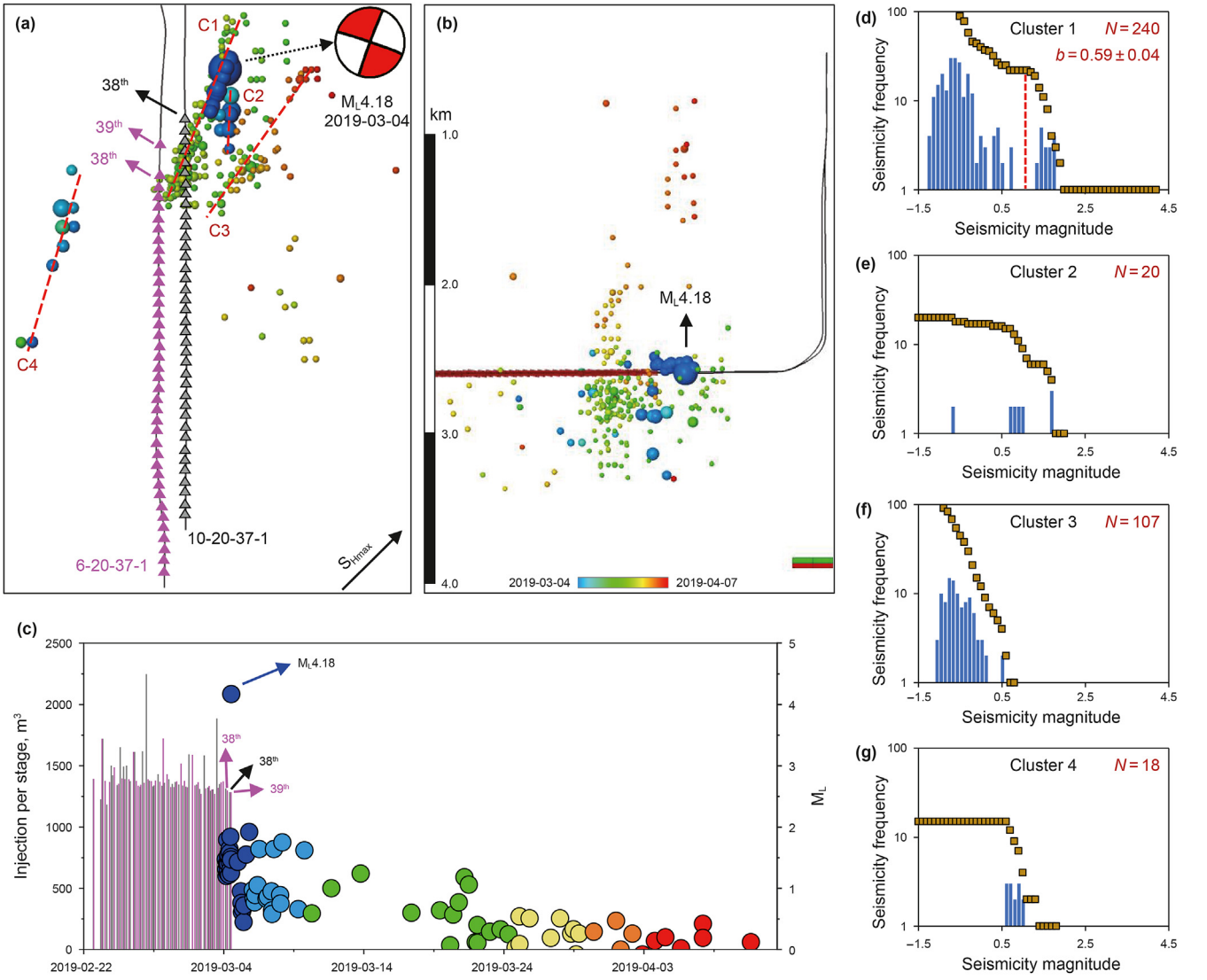

Fig. 2. Spatiotemporal view of the induced events and daily observation of HF operations in the M_L4.18 case. (**a**, **b**) Spatial view of magnitude-scaled event epicenters. The green circle represented the original focal hypocenter of the M_L4.18 event. (**c**) Daily observation of injection volume per stage and induced earthquakes. The grey and pink vertical lines denote the injection volume per stage for two horizontal wells. (**d**–**g**) The plots of seismicity frequency and magnitude in four clusters.

$$\phi = \frac{(\phi_{D\_sh} * \phi_{den}) / (\phi_{N\_sh} * \phi_{cnl})}{\phi_{D\_sh} - \phi_{N\_sh}}, \quad (1)$$

where ϕ is the formation porosity, %; ϕ_{D_sh} and ϕ_{N_sh} are the density porosity and neutron porosity of a pure shale point, respectively, %; ϕ_{den} and ϕ_{cnl} are the measured density porosity and neutron porosity, respectively, %.

Using the relationships between porosity and permeability as well as gas saturation, the petrophysical properties of other wells are determined. The sequential gaussian stochastic (SGS) method determines the petrophysical characteristics of the entire region, in which the spatial correlation between properties was considered via the searching neighborhood approach (Hui et al., 2021b).

3.3. 3D geomechanical modeling

A triaxial compression test (TCT) is used to determine the static rock mechanical properties of coring wells. Eqs. (2)–(4) are used to calculate the dynamic rock mechanical parameters from P-wave and S-wave logs (Pan et al., 2020; Pedersen et al., 2002; Yasin et al., 2021). The brittleness index (*BI*) is calculated based on the rock's mechanical parameters to evaluate the rock brittleness in shale reservoirs, and the SGS method is then applied to the entire region.

$$\nu = \frac{0.5(V_P/V_S)^2 - 1}{(V_P/V_S)^2 - 1}, \quad (2)$$

$$E = \rho V_S{}^2 \frac{3V_P{}^2 - 4V_S{}^2}{V_P{}^2 - V_S{}^2}, \quad (3)$$

$$BI = \omega \times \frac{\nu_{max} - \nu}{\nu_{max} - \nu_{min}} + (1 - \omega) \times \frac{E - E_{min}}{E_{max} - E_{min}}, \quad (4)$$

where V_S and V_P are S-wave velocity and P-wave velocity, respectively, m/s; ν, ν_{max}, and ν_{min} are measured, maximum, and minimum values of Poisson's ratio, respectively, dimensionless; E, E_{max}, and E_{min} are measured, maximum, and minimum values of Young's modulus, respectively, GPa; ρ is density, g/cm^3; ω is the weighting

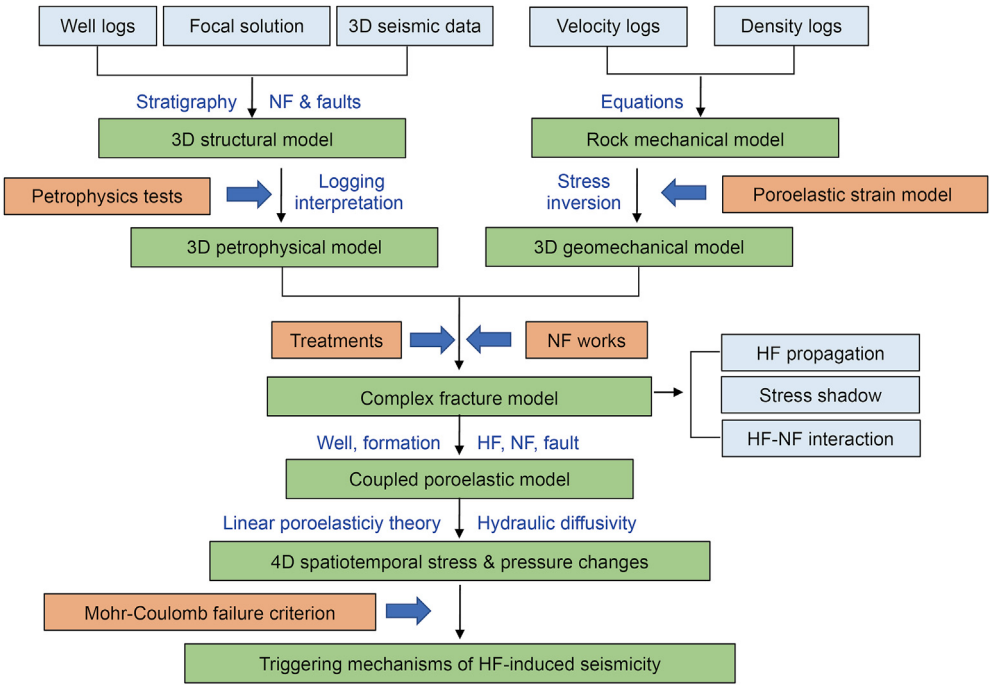

Fig. 3. The workflow of an integrated geoengineering evaluation of HF-induced earthquakes.

coefficient, assigned to 0.5 in this case.

For the full stress tensors and formation pressures, we employ Shen's stress and pressure model in this study region (Shen et al., 2021; Hui et al., 2022b). The data of formation pressure (P_p), vertical principal stress (V_p), minimum principal stress (S_{hmin}) and maximum principal stress (S_{Hmax}) covering the examined region is available through the online database (https://data.mendeley.com/datasets/tgmxx5vkjx/1).

3.4. Unconventional fracture modeling (UFM)

3.4.1. Hydraulic fracture propagation

The UFM is utilized to construct complex non-uniform fracture networks based on a geomechanical model and NF networks. UFM is also used in unconventional reservoirs to simulate the three-dimensional propagation of non-uniform hydraulic fractures. UFM is more applicable than a conventional pseudo-3D fracture model in resolving the problem of fluid flow and elastic deformations in hydraulic fracture networks. Eq. (5) below demonstrates the governing expressions of mass conservation (Weng et al., 2011), which is given by

$$\frac{\partial q}{\partial S}+\frac{\partial\left(H_{\mathrm{fl}} w_{\mathrm{avg}}\right)}{\partial t}+Q_{\mathrm{L}}=0 \quad\left(Q_{\mathrm{L}}=2 h_{\mathrm{lo}} u_{\mathrm{lo}}\right), \tag{5}$$

where q is the flow rate in a hydraulic fracture along the length of any fracture branch; w_{avg} is the average fracture width; H_{fl} is the fluid-filled fracture height; and Q_L is the product of leak-off height h_{lo} multiplying the leak-off velocity u_{lo} by Carter's leak-off model.

Darcy's flow and laminar flow characterize the rheological behavior of fluid during hydraulic fracturing beneath the ground. The laws that regulate these flows are defined by Eqs. (6) and (7) (Weng et al., 2014)

$$\frac{\partial p}{\partial S}=-\alpha_0 \frac{1}{\overline{w}^{2 n_0+1}} \frac{q}{H_{\mathrm{fl}}}\left|\frac{q}{H_{\mathrm{fl}}}\right|^{n_0-1} \quad \text{(Laminar)}, \tag{6}$$

$$\alpha_0=\frac{2 K_0}{\Phi\left(n_0\right)^{n_0}}\left(\frac{4 n_0+2}{n_0}\right)^{n_0} ; \quad \Phi\left(n_0\right)=\frac{1}{H_{\mathrm{fl}}} \int_{H_{\mathrm{fl}}}\left(\frac{w(z)}{\overline{w}}\right)^{\frac{2 n_0+1}{n_0}} \mathrm{d} z, \tag{7}$$

where n_0 and K_0 are a power-law index and a consistency index, respectively; $w(z)$ is the fracture width at a given depth, calculated by Eq. (10). The elastic law governs the width of a hydraulic fracture linked to fluid pressure.

Assume a vertical hydraulic crack in layered shale is subjected to normal stress I in the i^{th} layer. The stress intensity factors at the upper tip (K_{I_up}) and lower tip (K_{I_low}) can be calculated using the governing equation by Eq. (8) through Eq. (10) (Mack et al., 1992).

$$K_{\mathrm{I\_low}}=\sqrt{\frac{\pi h}{2}}\left[P_{\mathrm{cp}}-\sigma_{\mathrm{n}}+\rho_{\mathrm{f}} g\left(h_{\mathrm{cp}}-\frac{h}{4}\right)\right]+\sqrt{\frac{2}{\pi h}} \sum_{i=1}^{n-1}\left(\sigma_{i+1}-\sigma_i\right) \times\left[\frac{h}{2} \arccos\left(\frac{h-2 h_i}{h}\right)+\sqrt{h_i\left(h-h_i\right)}\right], \tag{8}$$

$$K_{\mathrm{I\_up}}=\sqrt{\frac{\pi h}{2}}\left[P_{\mathrm{cp}}-\sigma_{\mathrm{n}}+\rho_{\mathrm{f}} g\left(h_{\mathrm{cp}}-\frac{3}{4} h\right)\right]+\sqrt{\frac{2}{\pi h}} \sum_{i=1}^{n-1}\left(\sigma_{i+1}-\sigma_i\right) \times\left[\frac{h}{2} \arccos\left(\frac{h-2 h_i}{h}\right)-\sqrt{h_i\left(h-h_i\right)}\right], \tag{9}$$

$$w(z)=\frac{4}{E}\left[P_{cp}-\sigma_n+\rho_f g\left(h_{cp}-\frac{h}{4}-\frac{z}{2}\right)\right]\sqrt{z(h-z)}+\frac{4}{\pi E}\sum_{i=1}^{n-1}(\sigma_{i+1}-\sigma_i)\left[(h_i-z)\cosh^{-1}\frac{z\left(\frac{h-2h_i}{h}\right)+h_i}{|z-h_i|}+\sqrt{z(h-z)}\arccos\left(\frac{h-2h_i}{h}\right)\right], \tag{10}$$

where h_i is the distance from a fracture bottom tip to the top i^{th} layer; P_{cp} is the fluid pressure at a given depth of h_{cp}; ρ_f is the density of a fluid.

Furthermore, the total volume of fracturing fluids equals the fluid volume within hydraulic fracture networks, some of which leaks into the formation. Boundary conditions at fracture points are set to net pressure and zero flow rate. The following is the governing equation (Eq. (11)) (Weng et al., 2014):

$$\int_0^t q(t)\mathrm{d}t=\int_0^{L(t)}h(s,t)\overline{w}(s,t)\mathrm{d}s+\int_{H_L}\int_0^t\int_0^{L(t)}2\mu_L\mathrm{d}s\mathrm{d}t\mathrm{d}h_{lo}, \tag{11}$$

3.4.2. Stress shadow effects

The effects of "stress shadow" are related to the interactions of neighboring hydraulic fissures. Stress shadow effects must be quantified since they account for the non-uniform propagation of hydraulic cracks. The opening and shearing displacements of nearby hydraulic fractures, in particular, alter the stress tensors of a hydraulic fracture. We calculated the additional normal stresses (σ_n^i) and shear stress (τ_s^i) imparted to one hydraulic fracture as a result of the opening and shearing displacement discontinuities (D_n and D_s) of its nearby hydraulic fractures using Crouch and Starfield's model via Eqs. (12) and (13) (Weng et al., 2014).

$$\sigma_n^i=\sum_{j=1}^N A^{ij}C_{ns}^{ij}D_s^j+\sum_{j=1}^N A^{ij}C_{nn}^{ij}D_n^j, \tag{12}$$

$$\tau_s^i=\sum_{j=1}^N A^{ij}C_{ss}^{ij}D_s^j+\sum_{j=1}^N A^{ij}C_{sn}^{ij}D_n^j, \tag{13}$$

where A^{ij} is 3D correction factor, dimensionless; C^{ij} is 2D elastic influence coefficients, dimensionless. It is noted that the original stress field encircling each hydraulic crack is calculated at each time step, and the additional shear and normal stress are applied to it.

3.4.3. HF–NF interaction

The focal mechanisms of induced events contribute to a greater comprehension of pre-existing natural fracture networks with a maximum implicit fracture length of 50 m (Konstantinovskaya et al., 2021). A hydraulic fracture can be crossed, arrested by, or dilate pre-existing natural fractures. The average apertures ($\overline{W}$) of hydraulic fractures with half-length (L) and height (H) at an NF–HF junction site are computed by Eq. (14) (Valko and Economides, 1995)

$$\overline{W}=2.53\left[\frac{(1-\nu^2)q\mu_f L^2}{EH}\right]^{1/4}, \tag{14}$$

where q is the injection rate; μ_f is the fluid viscosity; ν is Poisson's ratio; and E is Young's modulus; H is the fracture height; L is the fracture half-length. Once fluids penetrate the NF, the average fluid pressure $p_{NF}(t)$ at a given time t can be calculated by Eq. (15) (Weng et al., 2011)

$$p_{NF}(t)=p_f\tanh\left(\sqrt{\frac{2k_{nf}p_f}{\mu b_s^2}t}\right) \tag{15}$$

where p_f is the fluid pressure at the tip of an HF; k_{nf} is the natural fracture permeability.

According to Eq. (15), it is shown that the fluid diffusion becomes very pervasive once fluids penetrate the natural fractures. On the basis of Eq. (5) through Eq. (15), a non-uniform unconventional fracture model can be constructed, taking into account the propagation of hydraulic fractures, the stress shadow effect between adjacent hydraulic fractures, and the interactions between hydraulic and natural fractures. The Petrel Kinetix software is used in this work to develop such a UFM.

3.5. Poroelastic modeling and Mohr-Coulomb criterion

This study employed the linear poroelasticity theory to guide coupled poroelastic modeling and quantify the physical process within the unconventional fracture networks during hydraulic fracturing (Wang and Kumpel, 2003). First, a propagating fluid pressure front from a source can be evaluated based on the aforementioned UFM modeling. Then, to characterize spatiotemporal Coulomb failure stress changes (ΔCFS), a coupled poroelastic model incorporating wells, a formation, fractures, and faults is constructed with the infinite element approach by Eq. (16) through Eq. (17) via the Comsol software (Hui et al., 2021d). After simulating the changes in pore pressure and *in situ* stress during HF operations, the Mohr-Coulomb failure criterion is typically used to determine the spatiotemporal activation of the associated faults (Catalli et al., 2013; King and Devès, 2015). The ΔCFS can be obtained further by means of Eq. (18) through Eq. (21). The underlying triggering mechanisms can be determined accordingly by comparing the spatiotemporal evolution of induced seismicity and quantified changes in stress and pressure (Hui et al., 2021b).

$$G\nabla^2\vec{u}+\frac{G}{1-2\nu}\nabla\epsilon-\alpha\nabla P_p=\vec{f}(\vec{x},t), \tag{16}$$

$$\frac{1}{M}\frac{\partial P_p}{\partial t}+\alpha\frac{\partial\epsilon}{\partial t}-\nabla\bullet\left(\frac{k}{\eta}\nabla P_p\right)=q(\vec{x},t), \tag{17}$$

$$\Delta CFS=(\Delta\tau-\mu\Delta\sigma_n)+\mu\Delta p_p, \tag{18}$$

$$\sigma_n{}'=\frac{1}{2}(\sigma_1+\sigma_3)-\frac{1}{2}(\sigma_1-\sigma_3)\cos(2\beta)-p_p, \tag{19}$$

$$\tau^l=\frac{1}{2}(\sigma_1-\sigma_3)\sin(2\beta), \tag{20}$$

$$\tau^r=-\frac{1}{2}(\sigma_1-\sigma_3)\sin(2\beta), \tag{21}$$

where G is the shear modulus; u is the displacement vector; ν is Poisson's ratio; ϵ is the volumetric strain; α is Biot's coefficient; $\vec{f}(\vec{x},t)$ is the body force per unit volume on the solid matrix; p_p is the pore pressure; M is the Biot modulus; k is the matrix permeability; η is the dynamic fluid viscosity; ρ is the fluid density; z is the measured depth; $q(\vec{x},t)$ is the volume injection source rate; Δ

denotes the changes in each parameter; *CFS* is the Coulomb failure stress; τ is the shear stress (positive in the slipping direction); σ_n' is the effective normal stress (positive in the extensional direction); μ is the friction coefficient; σ_1 and σ_3 are the magnitudes of S_{Hmax} and S_{hmin}, respectively; τ^r and τ^l are the shear stresses in the right-lateral and left-lateral motions of the fault, respectively; and β is the angle between the S_{Hmax} orientation and the fault strike (Hui et al., 2021e).

4. Results and discussion

4.1. Reservoir structure characterization

To conduct stratigraphic correlations, the available well logging data from six consecutive wells are gathered (Fig. 1c). Log characteristics (e.g., high gamma-ray and high formation resistivity) are utilized to locate the top and bottom of the Duvernay Formation. Accordingly, the elevation of the Duvernay Formation can be mapped using the SGS method (Fig. 1a). It is also noted that the carbonate component developed within the Duvernay Formation with relatively low gamma-ray and high formation resistivity.

In previous works, the available 3D seismic data is collected, attempting to determine the pre-existing faults associated with earthquake clusters (Fig. 4a–d) (Galloway et al., 2018; Galloway and Hauck, 2021). Seismic variations indicate that a basement-rooted fault (i.e., Fault 3) developed upwards to the Duvernay Formation (Fig. 4b and d). However, this inferred basement-rooted fault is not consistent with the distribution of induced events. This mismatch may be attributed to the relatively low resolution of 3D seismic data, which has been corroborated by previous works that not all inferred faults can be identified by the 3D seismic data (Atkinson et al., 2016).

Therefore, the focal mechanisms of induced events are used instead in our research to determine the associated seismogenic fault (Fig. 4e). The publicly available focal mechanisms of forty induced events are compiled, and the corresponding statistics are depicted in Fig. 4e. It is observed that, under the influence of two-period tectonics, the primary orientations of the natural fractures or faults were NE15° and SW285°. Image logs estimated the natural fracture intensity in terms of the ratio of a fracture area to volume to be 0.05 m^2/m^3 (Kleiner and Aniekwe, 2019). In addition, the spatial attributes of induced events can be used to improve the data quality of a pre-existing fault distribution because the other three faults are not readily apparent in the seismic attributes (Fig. 4a–d). Based on the inferred faults distribution and focal strike information (Wang et al., 2020), the fine structural model of the studied region is built by incorporating four inferred faults (i.e., Fault 1 through Fault 4) and two-period natural fracture networks (Fig. 4e), laying the foundation for the subsequent petrophysical modeling. It is worth noting that we chose from one of the two conjugate fault orientations (i.e., NE-SW orientation) from the focal solution as it follows with the distribution of the events.

4.2. Reservoir petrophysics characterization

The tight rock analysis (TRA) experiments are conducted on 84 core samples from three coring wells, and the results are collected from the publicly available database. According to a cross-plot between the density and neutron logs, we find that the rock density and neutron value at a shale point (i.e., 100 percent shale content) are 2.65 g/m^3 and 0.3, respectively (Fig. 5a). Then, Eq. (1) is used here to calculate the porosity of the shale, which corresponds to the measured effective porosity. In addition, it is observed that the permeability (k) of shale rocks has a positive logarithmic relationship with their effective porosity (ϕ), as shown by $k = 2 \times 10^{-6} e^{0.3104\phi}$ (Fig. 5b). Furthermore, the gas saturation (S_g) has a positive linear relationship with the petrophysical index (i.e., $(k\phi)^{0.5}$), given by $S_g = 1422.6(k\phi)^{0.5} + 2.9254$. This phenomenon can be attributed to the fact that the petrophysical index can be used as a proxy for pore size, which has been linked to the bound water within shale pores (Fig. 5c).

The SGS method allows for the construction of a petrophysical model using interpretation models of reservoir petrophysics and available well logs from straight wells. A cross-sectional view of shale porosity along the fracturing wells is depicted in Fig. 5d. The east well (10-20-37-1) targeted the upper Duvernay Formation, whereas the west well (6-20-37-1) targeted the Duvernay Formation 35 m below the east well. The gap between the target zones of these two wells will eliminate interference from other wells. It is also worth noting that, along the fracturing horizontal wells, the shale porosity has a sharp heterogeneity in the planar and vertical distribution, covering the range of 0.02–0.06 in magnitude. This type of spatial diversity may play a significant role in fluid diffusion during hydraulic fracturing.

4.3. 3D geomechanical characterization

Based on Eqs. (2)–(4), the rock mechanical properties of eight straight wells with P- and S-wave velocity logs are determined. The rock mechanical properties of straight wells are depicted in Fig. 6a. Poisson's ratio varies between 0.2 and 0.4, whereas Young's modulus varies between 20 and 80 GPa. Therefore, the brittleness index has a magnitude range of 0.1–0.9. The SGS method is utilized to obtain these properties for an entire region. The cross-sectional view of the brittleness index along the fractured wells is depicted in Fig. 6b. It is observed that the brittleness index (*BI*) along the two horizontal wells has a high magnitude ($BI > 0.5$), indicating the potential susceptibility of rock brittleness and providing the foundation for the formation of unconventional fracture networks.

The formation pressure (P_p) model is constructed, and the profile feature is depicted in Fig. 6c. Along the fractured wells, it is demonstrated that the Duvernay Formation has a higher formation pressure (46 MPa) than the DIreton Formation (43 MPa). Due to the presence of overpressure, pre-existing faults in the Duvernay Formation are highly susceptible to fault reactivation, as a small increase in pressure will cause a fault to enter the state of failure. In addition, the horizontal stress models are developed to determine the spatial distributions of the principal vertical stress (σ_v), minimum principal stress (σ_h), and maximum principal stress (σ_H). Similar to P_p, Fig. 6d demonstrates that the average σ_h within the Duvernay Formation (50.5 MPa) is greater than that of the DIreton Formation (47.5 MPa). It is also shown that σ_h has a sharp heterogeneity along the fractured wells, with the magnitude in the heel part (left) lower than the toe part (right). The formation pressure, as well as the stress model, can be used to evaluate the fault stability before and after hydraulic fracturing (Yew and Wei, 2015; Hui et al., 2021b).

4.4. UFM characterization

Based on the aforementioned structural, petrophysical, and geomechanical modeling, the complex fracture network modeling was carried out by Petrel KINETIX (https://www.software.slb.com/products/kinetix). Such software can be used to simulate hydraulic fracture propagation based on Eqs. (5)–(15), which has considered stress shadow effects between adjacent hydraulic fractures and natural-hydraulic fracture interactions. Table 1 shows the input geological, geomechanical and operational parameters associated

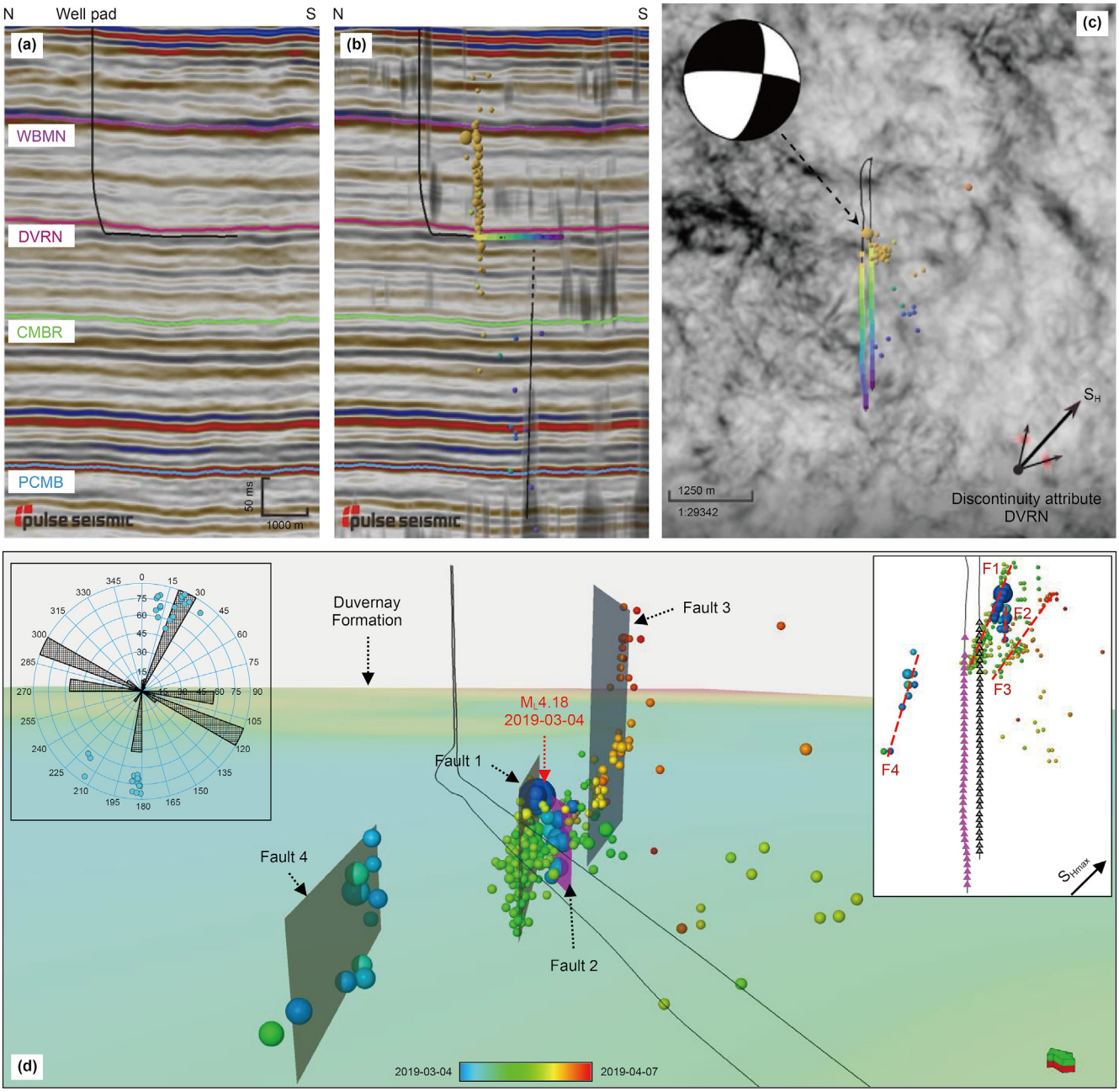

Fig. 4. Seismic interpretation and structural model. (**a**) Cross-section without interpretation. (**b**) Cross-section with seismic variance overlaid. An inferred basement-rooted fault developed upwards to Duvernay Formation. (**c**) The horizontal section shows the discontinuity attribute anomalies along the Duvernay Formation and Precambrian Basement. (**d**) 3D structural model. Four pre-existing faults are interpreted with high dip angles. Four clusters of induced earthquakes are spatially distributed surrounding four associated faults. Induced events are colored by time and scaled by magnitude. The left inset map shows the focal strike statistics of induced events, and the right inset map represents the view of four inferred faults.

with the UFM. The simulation results are illustrated in Fig. 7a–d (Hui et al., 2021d; Konstantinovskaya et al., 2021; Fothergill et al., 2014)). It is shown that as the 1st–37th stages of the west well 6-20-37-1 and east well 10-20-37-1 were completed, no pre-existing faults were reactivated, indicating no fault reactivation by that time.

However, when the 38th stage of the west well was completed with a total fracturing fluid injection of 1299 m^3 and an average rate of 15.2 m^3/min, the stimulated hydraulic fractures connected with Fault 1. Such a hydraulic connection caused Fault 1 to slip and triggered twelve induced earthquakes with a magnitude range of M1.2-M1.79 (Fig. 7a). Four hours later, the 38th stage completion of the east well was finished, pumped with a total fracturing fluid injection of 1284 m^3 and an average rate of 15.0 m^3/min. The associated hydraulic fractures also had a hydraulic communication with Fault 1, and five induced events (M1.3-M1.84) were monitored (Fig. 7b). As no large magnitude earthquakes occurred, the zip fracturing of both wells continued. Two hours later, the 39th stage of the west well was fractured with a total injection volume of 1202 m^3 and an average rate of 15.7 m^3/min. Besides leading to Fault 1 reactivation with a maximum M4.18-magnitude earthquake, the stimulated fractures also reactivated Fault 4 with a

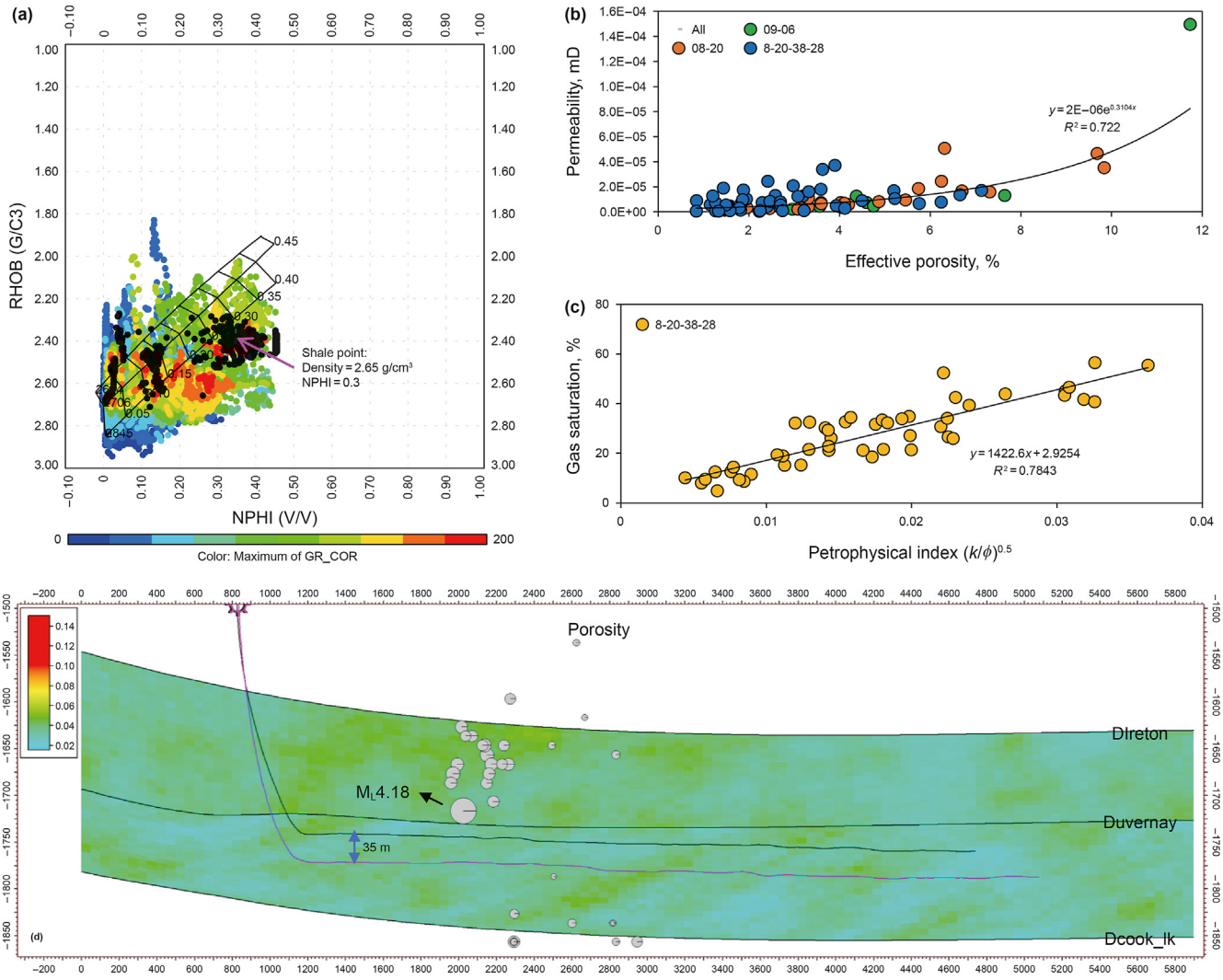

Fig. 5. (**a**) Cross-plot between rock density and neutron logs. (**b**, **c**) Relationship between geophysical properties. (**d**) A cross-sectional view along horizontal wells of formation properties. The induced earthquakes are overlaid in the profile.

maximum M1.75-magnitude earthquake (Fig. 7c). By 2019-04-07, 36 days after all completions, a fluid diffusion effect reactivated Fault 2 and Fault 3 and triggered other induced events with a magnitude range of M-1.41-M1.92 (Fig. 7d). The lineament trending of induced events also corroborated the reactivation of the associated pre-existing faults. The quantification of such HF-fault hydraulic connections will be discussed in the following sections.

4.5. Triggering mechanisms via coupled simulation

The coupled poroelastic model of the studied case is constructed based on Eqs. (16) and (17) via the COMSOL software (Hui et al., 2021b). Such a finite-element simulation is conducted by coupling solid mechanics with Darcy's law to characterize the spatiotemporal changes of poroelastic stress and pore pressure during HF operations. This block model is set with the dimensions of 4500 m × 4000 m × 550 m (Fig. 8a). The associated elements (e.g., faults, fractures, and wells) from the geological model are incorporated into the model (Fig. 8b). The boundary and initial conditions are also set based on the geological and geomechanical models and the actual treatment data. Finally, the Mohr-Coulomb failure criterion is utilized to determine the spatial-temporal faults activation based on Eq. (18) through Eq. (21). The details of the coupled poroelastic model have been well documented by our previous research (Hui et al., 2021d).

Consequently, the hydraulic connection between the hydraulic fractures of the east well and Fault 1 is quantified. The spatial distribution of Δ*CFS* at the cross point between fault and hydraulic fractures over time is shown in Fig. 9a and b. The induced events related to the east 38th stage completion are also displayed, scaled by seismicity magnitude (Fig. 9b). It is noted that the 32nd stage-related hydraulic fractures first connected Fault 1 (Fig. 9a). However, due to the slow diffusivity among a fault damage zone (Haddad and Eichhubl, 2020), the associated increase in pore pressure in this stage cannot reactivate Fault 1. However, when the hydraulic fractures at the 38th stage were connected Fault 1, the increase in pore pressure (ΔP_p) and Coulomb failure stress changes (Δ*CFS*) reached 6.06 and 3.94 MPa, respectively (Fig. 9b and c). The threshold value of Fault 1 (ΔP_{p0}) is obtained by moving the failure line to approach the fault state point (blue circle in Fig. 9d) and reading the value of the *x*-intersection point. Here, this value is found to be 1.8 MPa. Therefore, the increases in pore pressure (ΔP_p) exceeded the threshold value (ΔP_{p0}) required to reactivate Fault 1 (Fig. 9d). It is worth noting that, compared with poroelastic stress

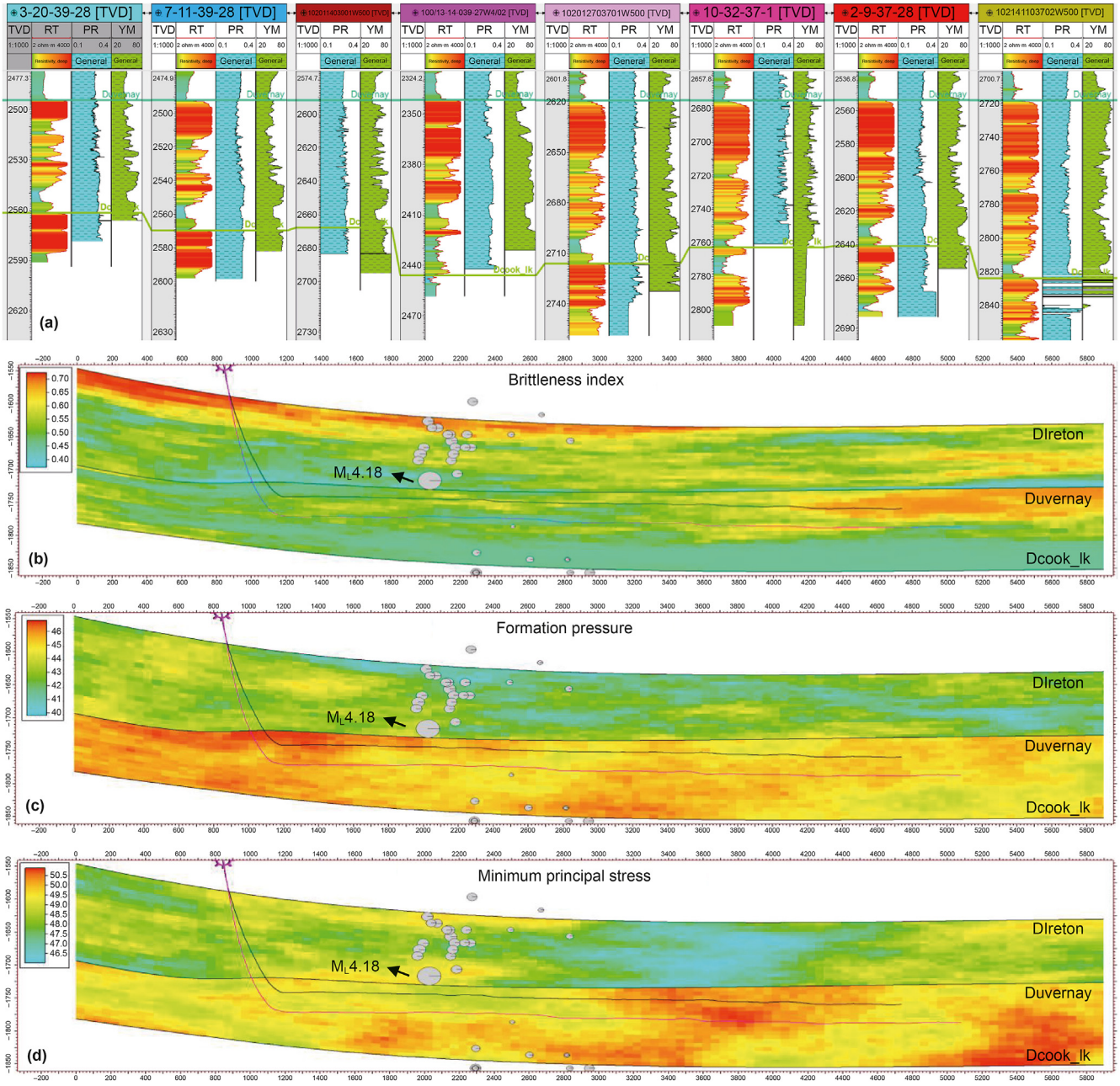

Fig. 6. (**a**) Rock mechanical properties of straight wells with velocity logs. These wells are shown in Fig. 1a. (**b**–**d**) A cross-sectional view along the fracturing wells of brittleness index, formation pressure, and minimum principal stress, respectively.

Table 1
Input data for unconventional fracture modeling.

Parameter		Value	Parameter		Value
Fluid	Viscosity	0.04 Pa s	Rock	Leak-off coefficient	3.9×10^{-2} m/s$^{1/2}$
	Density	1200 kg/m^3		Shale compressibility	4.6×10^{-10} Pa^{-1}
	Specific gravity	1.0			
Natural fracture	Toughness	1 MPa m$^{0.5}$	Fault	Fault normal/shear stress	6/3 GPa/m
	Orientation	NE15°/SW285°		Cohesion	0.1 MPa
	Length	A maximum of 50 m with a standard deviation of 10 m		Friction angle	22.5
	Spacing	A maximum of 100 m with a standard deviation of 10 m		Tensile strength	0.01

changes, the elevating pore pressure is the most significant factor that contributes most to the fault reactivation in the M_L4.18 case (Fig. 9c). Therefore, reducing the job size to decrease the potential elevating pore pressure along a fault plane is a possible mitigation strategy to reduce the potential seismic hazards.

Utilizing experimental-based UFM and coupled poroelastic

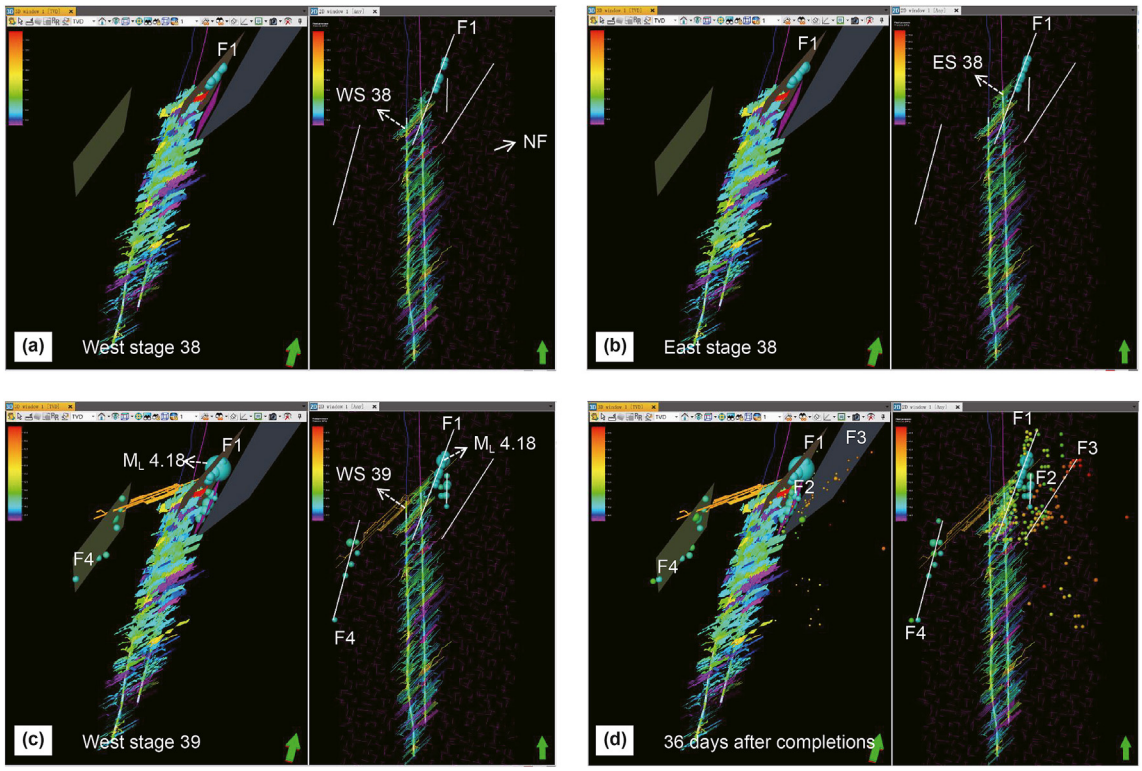

Fig. 7. (**a**–**c**) 3D and 2D view of the east well 38th stage completions, west well 38th stage completions and west well 39th stage completions and related induced events. (**d**) 3D and 2D view of hydraulic fractures and related induced events by 2019–04-07. The hydraulic fractures are colored by the magnitude of fluid pressure.

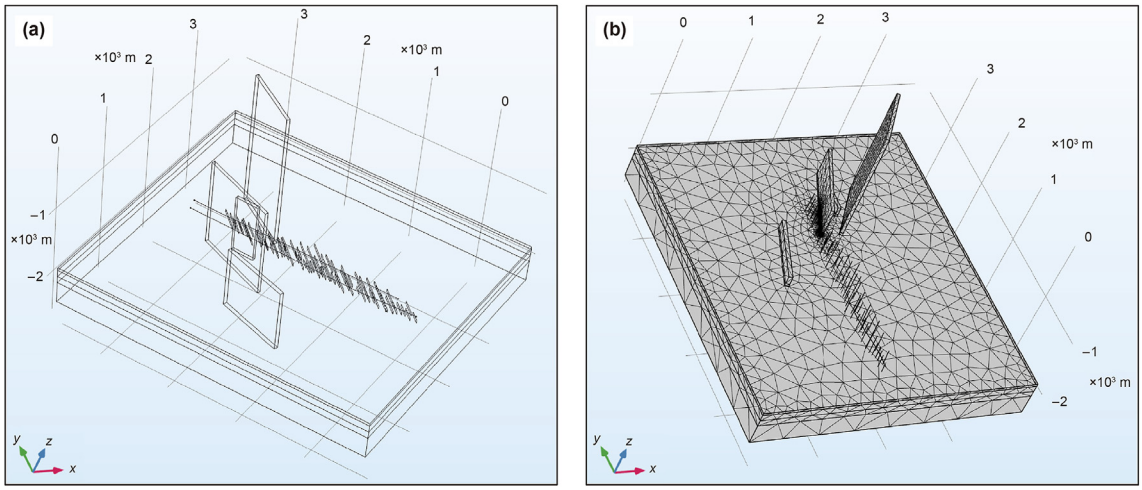

Fig. 8. (**a**) The coupled modeling. The block model is set with the dimension of 4500 m × 4000 m × 550 m with the associated elements (e.g., faults, fractures, and wells) from the geological model. (**b**) Mesh of the coupled model.

simulation, this study sheds light on the characterization of HF-induced earthquakes in the ESB. This workflow can be used to mitigate potential seismic risks in unconventional reservoirs in other fields. To construct reliable reservoir models and conduct numerical simulations, the primary objective of this work is to collect as much petrophysical and geomechanical experiment data from various coring wells, aiming to comprehensively characterize reservoir petrophysical and geomechanical characteristics (Baek and Jung, 2020; Sui et al., 2016). Additionally, this work also built UFM models considering the interactions between natural and hydraulic fractures, as well as stress shadows among the hydraulic fractures, which have not been fully investigated in prior induced seismicity studies (Weng et al., 2014). Furthermore, once new coring well data becomes available, a reservoir model should be updated to include these new data, which will provide a more robust database for subsequent UFM modeling. It is also noted that there are few studies of integrating and considering all structural, petrophysical, and geomechanical models when analyzing HF-induced earthquakes, though it is well acknowledged that both geological and engineering parameters have impacts on the mechanism of induced earthquakes, mainly because we do not have access to all these data. This work illustrates a good example

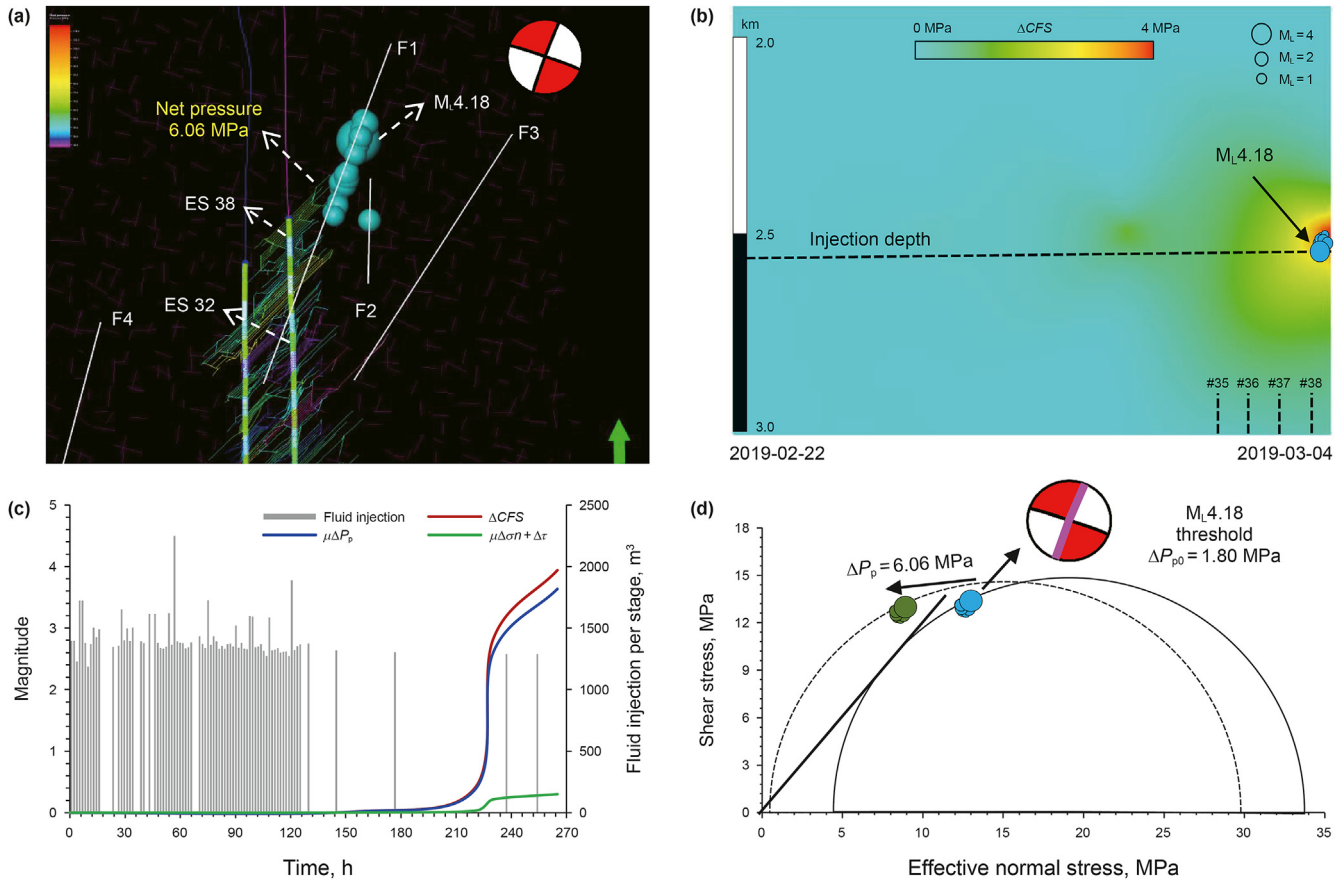

Fig. 9. The simulated results of coupled modeling in the reference case. (**a**) Horizontal cross-section view of ΔP_p at the top of Duvernay Formation using Petrel. (**b**) Spatial distribution of ΔCFS at the cross point between fault and hydraulic fractures over time. The induced events related to the east 38th stage completion are also displayed, scaled by seismicity magnitude. (**c**) Temporal distribution of ΔCFS, $\mu\Delta P_p$, $\mu\Delta\sigma_n + \Delta\tau$ at the cross point in the top Duvernay Formation. (**d**) Mohr circle showing the changes of shear stress and effective normal stress before (blue circles) and after (green circles) 38th stage completions.

to show what and how we can do when we have enough data in hand (Li et al., 2020). However, it is actually very difficult to directly replicate the proposed workflow to other fields if we do not have enough data.

This study also sheds light on the potential mitigation strategies for HF-induced seismicity in the development of unconventional resources. Specific to the M_L4.18 case, based on the simulation results, the east 32nd–38th stages and the west 38th–39th stages should not have been fractured to avoid the hydraulic connection between the hydraulic fractures and the nearby faults. Another mitigation method is to reduce the fracturing job size, that is, to reduce the fluid injection volume or treatment pressure so that the corresponding increase in pressure would have been less than the threshold of 1.80 MPa (Fig. 9d) (Mignan et al., 2019). Based on the coupled simulation, the limit injection volume to ensure that the increase in pore pressure will not exceed the threshold is 772 m^3 for the last stage of the well. Obviously, the first mitigation strategy would be more effective based on the prior field case studies (Hui et al., 2021c). This method can also be applied to other fields to lessen the potential seismic risks.

5. Conclusions

This paper proposes a novel synthetical geoengineering methodology to comprehensively characterize M_L4.18 earthquake clusters caused by hydraulic fracturing. Based on the 3D structural, petrophysical, and geomechanical models, the unconventional fracture model is constructed by considering the stress shadow between adjacent hydraulic fractures as well as the interactions between hydraulic and natural fractures. Coupled poroelastic simulations are conducted to reveal the triggering mechanisms of induced seismicity. The conclusions are drawn as follows.

(1) Four vertical basement-rooted faults were identified via focal mechanisms analysis. The primary orientations of the natural fractures or faults were determined to be NE15° and SW285°.
(2) The brittleness index (*BI*) along two horizontal wells had a high magnitude ($BI > 0.5$), indicating the potential susceptibility of rock brittleness. Due to the presence of overpressure, pre-existing faults in the Duvernay Formation were highly susceptible to fault reactivation, as a small increase in pressure caused a fault to enter the state of failure.
(3) The occurrence of earthquake clusters was attributed to the fracturing fluid injection during the west 38th–39th stage and east 38th stage completions. The increase in pore pressure (ΔP_p) and Coulomb failure stress changes (ΔCFS) reached 6.06 MPa and 3.94 MPa, respectively, exceeding the threshold value ($\Delta P_{p0} = 1.8$ MPa) to reactivate the pre-existing fault.
(4) Rock brittleness, formation overpressure, and large fracturing job size account for the nucleation of the earthquake clusters. Unconventional natural-hydraulic fracture

networks provide fluid flow pathways to cause the reactivation of the seismogenic fault.

Declaration of competing interest

The authors declare that they have no known competing financial interests or personal relationships that could have appeared to influence the work reported in this paper.

Acknowledgments

This research has been made possible by contributions from the Natural Sciences and Engineering Research Council (NSERC)/Energi Simulation Industrial Research Chair in Reservoir Simulation and the Alberta Innovates (iCore) Chair in Reservoir Modeling. This research was supported by Science Foundation of China University of Petroleum, Beijing (No. 2462023BJRC001) and National Natural Science Foundation of China Project (No. 52204039).

References

Alberta Energy Regulator, 2015. Subsurface order no. 2: monitoring and reporting of seismicity in the vicinity of hydraulic fracturing operations in the Duvernay zone, Fox Creek, Alberta. In: AER Bulletin 2015–07.

Anyim, K., Gan, Q., 2020. Fault zone exploitation in geothermal reservoirs: production optimization, permeability evolution and induced seismicity. Advances in Geo-Energy Research 4 (1), 1–12. https://doi.org/10.26804/ager.2020.01.01.

Atkinson, G.M., Eaton, D.W., Ghofrani, H., et al., 2016. Hydraulic fracturing and seismicity in the Western Canada sedimentary basin. Seismol Res. Lett. 87 (3), 631–647. https://doi.org/10.1785/0220150263.

Baek, W.K., Jung, H.S., 2020. Precise three-dimensional deformation retrieval in large and complex deformation areas via integration of offset-based unwrapping and improved multiple-aperture SAR interferometry: application to the 2016 Kumamoto earthquake. Engineering 6 (8), 927–935. https://doi.org/10.1016/j.eng.2020.06.012.

Catalli, F., Meier, M.A., Wiemer, S., 2013. The role of Coulomb stress changes for injection-induced seismicity: the Basel enhanced geothermal system. Geophys. Res. Lett. 40, 72–77. https://doi.org/10.1029/2012GL054147.

Chen, J., Wang, L., Wang, C., et al., 2021. Automatic fracture optimization for shale gas reservoirs based on gradient descent method and reservoir simulation. Advances in Geo-Energy Research 5 (2), 191–201. https://doi.org/10.46690/ager.2021.02.08.

Ellsworth, W.L., 2013. Injection-induced earthquakes. Science 341, 1225942. https://doi.org/10.1126/science.1225942.

Eyre, T.S., Eaton, D.W., Garagash, D.I., et al., 2019. The role of aseismic slip in hydraulic fracturing-induced seismicity. Sci. Adv. 5 (8), eeav7172. https://doi.org/10.1126/sciadv.aav7172.

Fothergill, P., Boskovic, D., Schoellkopf, N., et al., 2014. Regional modelling of the late devonian Duvernay Formation, western Alberta, Canada. In: SPE/AAPG/SEG Unconventional Resources Technology Conference. https://doi.org/10.15530/URTEC-2014-1923935.

Galloway, E., Hauck, T., Corlett, H., et al., 2018. Faults and associated karst collapse suggest conduits for fluid flow that influence hydraulic fracturing-induced seismicity. Proc. Natl. Acad. Sci. USA 115 (53), E10003–E10012. https://doi.org/10.1073/pnas.1807549115.

Galloway, E.J., Hauck, T.E., 2021. Insights into induced seismicity in the Duvernay East Shale basin from 3D seismic. Geoconvention 2021.

Ghofrani, H., Atkinson, G.M., 2020. Activation rate of seismicity for hydraulic fracture wells in the western Canada sedimentary basin. Bull. Seismol. Soc. Am. 110 (5), 2252–2271. https://doi.org/10.1785/0120200002.

Haddad, M., Eichhubl, P., 2020. Poroelastic models for fault reactivation in response to concurrent injection and production in stacked reservoirs. Geomechanics for Energy and the Environment 24, 100181. https://doi.org/10.1016/j.gete.2020.100181.

Hui, G., Chen, S., He, Y., et al., 2021a. Production forecast for shale gas in unconventional reservoirs via machine learning approach: case study in Fox Creek, Alberta. J. Nat. Gas Sci. Eng. 94, 104045. https://doi.org/10.1016/j.jngse.2021.104045.

Hui, G., Chen, S., Chen, Z., et al., 2021b. Comprehensive characterization and mitigation of hydraulic fracturing-induced seismicity in Fox Creek, Alberta. SPE J. 26 (5), 2736–2747. https://doi.org/10.2118/206713-PA.

Hui, G., Chen, S., Chen, Z., et al., 2021c. Influence of hydrological communication between basement-rooted faults and hydraulic fractures on induced seismicity: a case study. J. Petrol. Sci. Eng. 206, 109040. https://doi.org/10.1016/j.petrol.2021.109040.

Hui, G., Chen, S., Chen, Z., et al., 2021d. Investigation on two Mw 3.6 and Mw 4.1 earthquakes triggered by poroelastic effects of hydraulic fracturing operations near Crooked Lake, Alberta. J. Geophys. Res. Solid Earth 126, e2020JB020308. https://doi.org/10.1029/2020JB020308.

Hui, G., Chen, S., Chen, Z., et al., 2021e. Role of fluid diffusivity in the spatiotemporal migration of induced earthquakes during hydraulic fracturing in unconventional reservoirs. Energy Fuels 35 (21), 17685–17697. https://doi.org/10.1021/acs.energyfuels.1c02950.

Hui, G., Chen, Z., Chen, S., et al., 2022a. Hydraulic fracturing-induced seismicity characterization through coupled modeling of stress and fracture-fault systems. Advances in Geo-Energy Research 6 (3), 269–270. https://doi.org/10.46690/ager.2022.03.11.

Hui, G., Chen, Z., Wang, Y., et al., 2023. An integrated machine learning-based approach to identifying controlling factors of unconventional shale productivity. Energy 266, 126512. https://doi.org/10.1016/j.energy.2022.126512.

Hui, G., Chen, Z., Wang, P., et al., 2022b. Mitigating risks from hydraulic fracturing-induced seismicity in unconventional reservoirs: case study. Sci. Rep. 12, 12537. https://doi.org/10.1038/s41598-022-16693-3.

Hui, G., Gu, F., 2022. An integrated method to mitigate hazards from hydraulic fracturing–induced earthquakes in the Duvernay Shale Play. SPE Res. Eval. Eng. https://doi.org/10.2118/210287-PA.

King, G.C.P., Devès, M., 2015. Fault interaction, earthquake stress changes, and the evolution of seismicity. Treatise on Geophysics 2 (4), 243–272.

Kleiner, S., Aniekwe, O., 2019. The Duvernay Shale completion journey. In: SPE Kuwait Oil & Gas Show and Conference. https://doi.org/10.2118/198070-MS.

Konstantinovskaya, E., Li, Q., Zhmodik, A., et al., 2021. Lateral fluid propagation and strike slip fault reactivation related to hydraulic fracturing and induced seismicity in the Duvernay Formation, Fox Creek area, Alberta. Geophys. J. Int. 227 (1), 518–543. https://doi.org/10.1093/gji/ggab234.

Li, L., Tan, J., Schwarz, B., et al., 2020. Recentadvances and challenges ofwaveform-based seismic locationmethods at multiple scales. Rev. Geophys. 58, e2019RG000667. https://doi.org/10.1029/2019RG000667.

Lei, X., Huang, D., Su, J., et al., 2017. Fault reactivation and earthquakes with magnitudes of up to Mw4.7 induced by shale-gas hydraulic fracturing in Sichuan Basin, China. Sci. Rep. 7, 7971. https://doi.org/10.1038/s41598-017-08557-y.

Lyster, S., Corlett, H.J., Berhane, H., 2017. Hydrocarbon Resource Potential of the Duvernay Formation in Alberta - Update. Alberta Energy Regulator, Edmonton, pp. 31–43.

Mack, M.G., Elbel, J.L., Piggott, A.R., 1992. Numerical representation of multilayer hydraulic fracturing. 33rd US Symposium on Rock Mechanics, Santa Fe, 3-5 June 1992 325-333.

Mignan, A., Karvounis, D., Broccardo, M., et al., 2019. Including seismic risk mitigation measures into the Levelized Cost of Electricity in enhanced geothermal systems for optimal siting. Appl. Energy 238, 831–850. https://doi.org/10.1016/j.apenergy.2019.01.109.

Pan, X., Zhang, G., Chen, J., 2020. The construction of shale rock physics model and brittleness prediction for high-porosity shale gas-bearing reservoir. Petrol. Sci. 17, 658–670. https://doi.org/10.1007/s12182-020-00432-2.

Pawley, S., Schultz, R., Playter, T., et al., 2018. The geological susceptibility of induced earthquakes in the Duvernay play. Geophys. Res. Lett. 45 (4), 1786–1793. https://doi.org/10.1002/2017GL076100.

Pedersen, S.I., Randen, T., Sonneland, L., Steen, O., 2002. Automatic 3D fault interpretation by artificial ants. 64th Meeting, EAEG Expanded Abstracts G037. https://doi.org/10.1190/1.1817297.

Rokosh, C.D., Lyster, S., Anderson, S.D.A., et al., 2012. Summary of Alberta's shale- and siltstone-hosted hydrocarbon resource potential. Energy Resources Conservation Board, ERCB/AGS Open File Report 2012-06 327.

Schultz, R., Atkinson, G., Eaton, D.W., et al., 2018. Hydraulic fracturing volume is associated with induced earthquake productivity in the Duvernay play. Science 359 (6373), 304–308. https://doi.org/10.1126/science.aao0159.

Schultz, R., Skoumal, R.J., Brudzinski, M.R., et al., 2020. Hydraulic fracturing-induced seismicity. Rev. Geophys. 58, e2019RG000695. https://doi.org/10.1029/2019RG000695.

Schultz, R., Wang, R., 2020. Newly emerging cases of hydraulic fracturing induced seismicity in the Duvernay East Shale Basin. Tectonophysics 779, 228393. https://doi.org/10.1016/j.tecto.2020.228393.

Shen, L.W., Schmitt, D.R., Wang, R., Hauck, T.E., 2021. States of in situ stress in the Duvernay East Shale Basin and willesden green of Alberta, Canada: variable in situ stress states effect fault stability. J. Geophys. Res. Solid Earth 126, e2020JB021221. https://doi.org/10.1029/2020JB021221.

Shen, L., Schmitt, D.R., Haug, K., 2019. Quantitative constraints to the complete state of stress from the combined borehole and focal mechanism inversions: Fox Creek, Alberta. Tectonophysics 764, 110–123. https://doi.org/10.1016/j.tecto.2019.04.023.

Sui, L., Ju, Y., Yang, Y., et al., 2016. A quantification method for shale fracability based on analytic hierarchy process. Energy 115, 637–645. https://doi.org/10.1016/j.energy.2016.09.035.

Tan, Y., Hu, J., Zhang, H., et al., 2020. Hydraulic fracturing induced seismicity in the southern sichuan basin due to fluid diffusion inferred from seismic and injection data analysis. Geophys. Res. Lett. 47 (4), e2019GL084885. https://doi.org/10.1029/2019GL084885.

Valko, P., Economides, M.J., 1995. Hydraulic Fracture Mechanics. John Wiley & Sons.

Wang, B., Harrington, R., Liu, Y., et al., 2020. A study on the largest hydraulic-fracturing-induced earthquake in Canada: Observations and static stress-drop estimation. Bull. Seismol. Soc. Am. https://doi.org/10.1785/0120190261.

Wang, R., Kumpel, H.J., 2003. Poroelasticity: efficient modeling of strongly coupled, slow deformation processes in multilayered half-space. Geophysics 68 (2), 1–13. https://doi.org/10.1190/1.1567241.

Weng, X., Kresse, O., Chuprakov, D., et al., 2014. Applying complex fracture model and integrated workflow in unconventional reservoirs. J. Petrol. Sci. Eng. 124, 468–483. https://doi.org/10.1016/j.petrol.2014.09.021.
Weng, X., Kresse, O., Cohen, C., Wu, R., Gu, H., 2011. Modeling of hydraulic fracture network propagation in a naturally fractured formation. In: SPE Hydraulic Fracturing Conference and Exhibition. https://doi.org/10.2118/140253-MS.
Yasin, Q., Sohail, M.G., Liu, K.Y., et al., 2021. Study on brittleness templates for shale gas reservoirs-A case study of Longmaxi shale in Sichuan Basin, southern China. Petrol. Sci. 18, 1370–1389. https://doi.org/10.1016/j.petsci.2021.09.030.
Yew, C.H., Wei, X., 2015. Mechanics of Hydraulic Fracturing, second ed. Gulf Professional Publishing.
Zhang, H.L., David, W.E., German, R., Suzie, Q.J., 2019. Source-mechanism analysis and stress inversion for hydraulic-fracturing-induced event sequences near Fox Creek, Alberta. Bull. Seismol. Soc. Am. 109 (2), 636–651. https://doi.org/10.1785/0120180275.
Zoback, M., 2007. Reservoir Geomechanics. Cambridge University Press, Cambridge.